Three-Dimensional Microstructural Analysis for the Characterization of Failure Mechanisms of a Novel SOEC

L. Wehner[a], C. Lenser[b], K. Dzieciol[c], E. Wessel[a], J. Malzbender[a], R. Schwaiger[a]

[a] Institute for Energy and Climate Research, Structure and Function of Materials (IEK-2)
Forschungszentrum Jülich GmbH, 25425 Jülich, Germany
[b] Institute for Energy and Climate Research, Materials Synthesis and Processing (IEK-1),
Forschungszentrum Jülich GmbH, 25425 Jülich, Germany
[c] Institute for Energy and Climate Research, Fundamental Electrochemistry (IEK-9),
Forschungszentrum Jülich GmbH, 25425 Jülich, Germany

A novel fuel electrode-supported electrolysis cell has been developed as promising candidate for hydrogen production at intermediate temperatures. It contains a Ni-GDC electrode functional layer, a three-layer GDC-YSZ-GDC electrolyte and an LSC air electrode. Although this cell enables improved performance compared to state-of-the-art YSZ electrolyte-based cells, especially at lower operation temperatures, 700 °C and below, and electrolysis currents around 1.2-1.7 A cm^{-2} a voltage drop and subsequently crack formation in the electrolyte was observed in initial studies. In the current work, FIB/SEM and X-ray computed tomography are used for microstructural investigations. Based on calculated microstructural parameters the suitability of the methods for an assessment of the failure mechanisms are discussed.

Introduction

Solid Oxide Electrolysis Cells (SOECs) are promising for the production of green hydrogen. State-of-the-art solid oxide cells utilize a Ni-YSZ cermet electrode and a YSZ electrolyte. However, the replacement of the Ni-YSZ functional layer by Ni-GDC for electrolyte and metal supported cells has been discussed in the literature.(1)

Recently, a novel fuel electrode supported SOEC containing a three-layer GDC-YSZ-GDC electrolyte and a Ni-GDC fuel electrode functional layer (CFL) has been developed. The doped-ceria based electrolyte circumvents the formation of low conductive oxides caused by interdiffusion between ceria and zirconia during the co-sintering of the electrode and electrolyte layer that otherwise would lead to a reduced performance.(2)

In fact, the cell showed excellent performance in a temperature range between 700 and 800 °C with no obvious signs of degradation at 750 °C and 800 °C. At lower temperatures, 700 °C and below, a voltage drop at high electrolysis currents and a drastic decrease in the OCV were observed, both indicating damage in the cell. A post-test analysis of the cells revealed the formation of an in-plane through thickness network of cracks in the electrolyte layer.(1)

Beside thermal stresses resulting from mismatches of the materials' thermal expansion coefficients additional stresses from chemical expansion of ceria under reducing conditions occurred. A gradient of the oxygen chemical potential along the electrolyte layer thickness caused by different oxygen partial pressures at both electrodes led to a gradient in the chemical expansion.(1) The combination of the thermally and chemically induced stresses led to the observed failure.

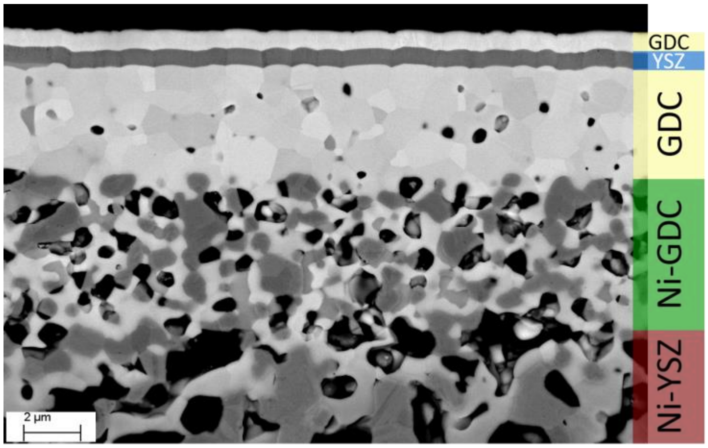

Figure 1: The cross-section of the cell shows the fuel electrode, including substrate and functional layer, and the three-layer electrolyte.

Three-dimensional microstructural investigations pre and post single cell testing under different operation conditions are suggested to provide an insight into microstructural changes related to testing conditions, and thus their failure relevance. The microstructure reconstructions will be a basis for future advanced simulations of the local stress distribution, and its relationship to microstructure and operation conditions. (3) The LSC electrode's effect on the mechanical behavior is assumed to be small due to its very porous structure, and therefore it will not be included into the investigations.

Microstructural characterization

Focused Ion Beam Tomography

Dual beam focused ion beam (FIB)/scanning electron microscopy (SEM) tomography is a powerful technique for the three-dimensional investigation of microstructures. Alternating FIB milling and SEM imaging combined with subsequent image processing yield three-dimensional data on microstructures. Several groups have reported the successful reconstruction and analysis of different cell components. For SOC materials routines were developed to investigate electrodes, electrolyte and substrates. Infiltration of the porous samples with an epoxide resin has been reported to facilitate the assignment of pore areas due to the resin's low brightness in the SEM images.(4, 5)

To yield statistical relevant microstructural parameters a minimum reconstructed volume and resolution are required. Joos et al. showed that a resolution of 20-30 voxels per particle diameter were necessary for porous LSCF electrodes. Lower resolutions did not lead to convergence in calculated parameters and thus are not reliable. The representative volume element (RVE) is the minimum volume size necessary for the reconstruction to be statistical representative for a sample. It mostly depends on the homogeneity of the specimen.(6) From the reconstruction calculated microstructural parameters such as surface area, tortuosity, volume fractions, etc. differ in their sensitivity on the volume size.

In literature the successful reconstruction of several SOC materials has been reported. Microstructures and related parameters of Ni-YSZ cermet fuel electrodes, YSZ based electrolytes as well as air electrodes were investigated. (4, 7–10)

Computed Tomography

X-ray computed tomography enables the non-destructive investigation of a sample. Depending on the materials included in the sample, volumes in an order of magnitude of 10^6 μm^3 can be investigated.(11) Scan results are mostly influenced by the analyzed sample itself. Dense materials show a stronger absorption of X-rays, and thus influence the scan results if in the beam's path. Additionally, they might lead to shadowing effects in their surrounding areas. With increasing density, the grayscale value also increases (0→250).(8)

The resolution is limited by different factors. Phases with similar atomic numbers or X-ray absorption coefficients are not distinguishable. Feature size is another limiting factor. Edges such as phase interfaces appear blurred in the scan. This effect is stronger the smaller the particles or phases. Although filtering steps can be applied to the data, boundaries will only be approximated. This results in uncertainties or even errors during the segmentation process. Phases and features that are smaller than the resolution limit cannot be identified.(8)

The successful reconstruction of cell components such as substrate material, Ni-YSZ cermet, and LSM electrodes has been reported. The resolution could be enhanced by utilizing different detectors for the materials.(5)

Image processing

In gray scale images there are distributions of gray scale values for the different materials rather than discrete values. Depending on the phase or material contrast, if the histogram is plotted, the peaks are not clearly separable but overlap to a certain degree. During the segmentation this would lead to errors in the assignment of voxels to the material phases. To reduce errors and ensure sufficient quality of the results separated histogram peaks are desired. Image quality can be enhanced by applying different filtering steps. However, too many filtering steps can alter the structure significantly, and may therefore lead to incorrect microstructures.(10, 11)

Due to shadowing effects brightness gradients might occur in image series recorded via FIB/SEM, caused by the increasing distance of image plane with proceeding milling process. The presence of brightness gradients is determined from the images' histograms. Those gradients can be removed by adjusting the brightness of slices in all three directions (x, y, z). Therefor the mean gray scale value for every slice is calculated and the difference to either the value of the whole image stack or one reference image is added to the whole histogram.

Reduction of noise was reported via different smoothing filters modeling diffusion processes.(12, 13) The smoothing extend depends on the surrounding areas, specifically on the distance to phase boundaries. Closer to edges the smoothing decreases in order to preserve edges and prevent blurring of different material phases which otherwise would lead to segmentation errors.

Segmentation

To obtain a three-dimensional material distribution each voxel of the reconstructed volume is assigned to one of the material phases based on its gray scale value and surrounding voxels. This procedure is called segmentation, and different methods have been discussed in literature.

The most intuitive method is the threshold-based segmentation. Each peak in the images' histogram is assigned to one of the samples phases. The gray scale values of the minima between the peaks are the threshold values for the segmentation. This method is an easy and fast way for images containing two clearly separable phases. If the histogram peaks partially overlap, errors in the assignment of voxels in the overlapping area may occur. In this case filtering of the images prior to segmentation might reduce the overlap and lead to more defined peaks. Different algorithms have been reported to determine threshold values.(14)

The hysteresis segmentation utilizes two threshold values that are both set to values that every pixel darker than g1 is assigned to phase 1 and pixels lighter than g2 are assumed to belong to phase 2. This leaves pixels with gray scale values corresponding to the overlapping part in the histogram unassigned. In a second step an iterative three-dimensional expansion of the assigned into unassigned regions is executed. The expansions terminate if either the regions are in contact or the next threshold value is reached.(11)

Another approach Ender et al. developed for overlapping histogram peaks is the local threshold method. The reconstructed volume is divided in smaller cubes for which threshold values then are determined. An interpolation of these values yields local threshold values for each voxel. The assignment afterwards is executed based on these. Thereby brightness gradients within the reconstructed volume do not lead to errors during the segmentation process.(12)

If an image stack contains more than two phases threshold-based segmentation often leads to errors in the material distribution. This is due to the limited resolution of the SEM. At the interfaces of the phases with the brightest and the darkest material contrast a few pixels are of an intermediate gray scale value. During the segmentation process these will be assigned to the material whose gray value lies in between the other phases. To prevent this the region-growing method was developed. A few voxels that certainly belong to a specific phase are assigned based on their gray scales. They function as seeds, and start growing by assignment of neighboring voxels in a next step. An edge map, that contains the phase boundaries, ensures that there is now growing into other phases. The probability of a voxel belonging to a certain phase strongly depends on the surrounding areas.(9)

Gray scale images may also be interpreted as topographic reliefs with every pixels' gray scale value being its height on an image plane. In the topography, beside minima and maxima, waterlines exist which are calculated during the watershed segmentation. If the image is flooded, starting from local minima, the waterlines are defined as edges where the flooded regions touch. A huge advantage of the watershed segmentation is its simplicity, wide field of application, and possibility of closed contour generation. The latter is especially for images with low contrast advantageous. On the downside, the segmentation is sensitive to noise, and tends to over segment if fluctuations in gradient magnitude exist. (15, 16)

Experimental

For the three-dimensional reconstruction FIB/SEM and CT were used. The analyzed volumes contained the three-layer electrolyte and the fuel electrode functional layer.

A sample of approximately 20 µm edge length was cut out of the cell via FIB and placed on a needle for the CT measurement. The reconstructed volume was 3489 µm^3. A XRADIA Ultra 810 (Carl Zeiss X-Ray Microscopy Inc., Pleasanton, USA) with an energy of 5.4 keV was used. To ensure a sufficient resolution (voxel size 65 nm) 721 projections were performed with an exposure time of 200 s.

FIB/SEM tomography was carried out with a DualBeam ZEISS Auriga (Carl Zeiss Microscopy GmbH, Oberkochen, Germany). To protect the cells microstructure while milling the volume for analysis was covered with platinum. Reference marks were cut into to Pt-layer to facilitate slice alignment during the reconstruction. To reduce shadowing effects at the edges of the cross-sectional images the VOI was cut free. A series of 74 consecutive images resulting in a volume of 1060 µm^3 was recorded using an Inlens EsB detector. A milling current of 2 nA at 30 kV was used for the cut and slice procedure.

To enhance the images' contrast the ImageJ Fiji distribution (17) was used. Avizo (version 9.0.0, Thermo Fisher Scientific Inc., Waltham, Massachusetts, USA) was utilized for the reconstruction process including alignment, filtering and segmentation of the FIB/SEM and CT data. It was also used for the determination of microstructural parameters.

Results and Discussion

FIB/SEM

After the alignment of the 74 slices a region of 10.6 µm by 11.2 µm was cut in the image plane. In this area no large shadowing or milling artefacts were present. The phases of the CFL were homogeneous distributed.

In the electrolyte layer sporadic areas of $GdPO_4$ were found. They were most likely formed during the co-sintering of the half-cell in a reaction between GDC and the phosphorus from the dispersant agent. The secondary phase was also present in the functional layer, but due to limits of the available detector, and therefore the material contrast, it was not distinguishable from the Ni. For this reason, no calculations of microstructural parameters for the Ni phase were conducted from this reconstruction. Apart from that no mayor defects such as cracks were found.

The GDC electrolyte layer was not fully dense but exhibits pores. The porosity was about 3.2 %. The pore tortuosity, calculated by the centroid path method in the layer, of 16.4 indicated that the pores did not form a pore network, and thus no pathway through the electrolyte. Therefore, no leakage was to be expected, which fits the cells good performance above 750 °C.(1)

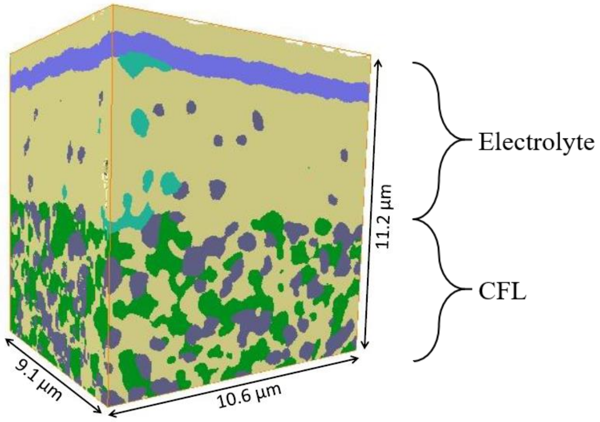

Figure 2: Material distribution in the reconstructed volume (1060 µm^3). No mayor defects but the formation of a $GdPO_4$ phase could be observed. Green: Ni; cyan: $GdPO_4$; purple: YSZ; yellow: GDC; gray: pores.

The porosity within the electrode functional layer was calculated to be 23.0 %. The theoretical possible porosity, which was determined from the NiO fraction of 0.5 used for the cells' fabrication, was 20.4 %. Considering inaccuracies in the segmentation process, due to not infiltrated pores and contrast at phase interfaces, the calculated porosity value agrees well with the theoretical value. The tortuosity value was determined using a centroid path tortuosity algorithm. The calculated value of 6.4 for the pores indicated a good connection of the network. For smaller analyzed volumes the value was greater. It might still decrease when the reconstructed volume will be enlarged. For the GDC the calculated volume fraction (37.9 %) was smaller than the theoretical value, which was expected to be 50 %. The $GdPO_4$ was not considered in the calculation of the theoretical volume fraction. The determined tortuosity value was 4.3. The smaller the tortuosity the better the connection of the phases.

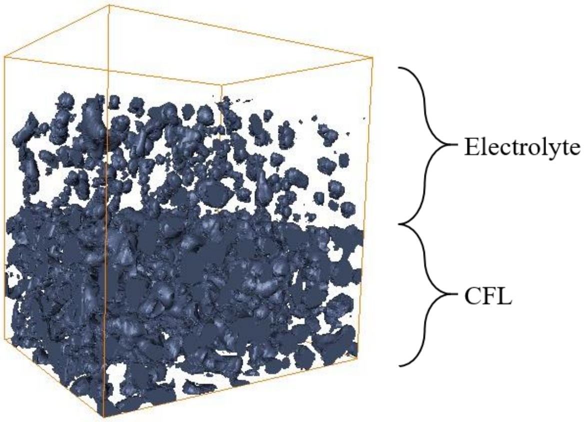

Figure 3: Distribution of pores in the CFL and electrolyte layer of the reconstructed volume (1060 µm^3).

The analysis of smaller sample volumes resulted in higher porosities and tortuosity values emphasizing the importance of a large enough volume to be statistically representative. The presence of the $GdPO_4$, especially the sporadic regions in the electrolyte layer, increased inhomogeneity of the cell. This might lead to an even larger RVE.

CT

The resolution of the scan was limited to distinguish only between pores and the material phases. This was due the fine material distribution and small grain sizes. Strong brightness and contrast enhancement were necessary to run the segmentation algorithm. The pore sizes in the electrolyte layer were mostly smaller than the pores in the CFL and substrate layer, and thus not all were visible. Hence, microstructural analysis was limed to the electrode.

The calculated porosity of the CFL was 24.1 %, and thus similar to the value obtained from the FIB/SEM data. It deviated a little more from the theoretical value, which was possibly caused by the resolution limit. Very small pores might have not been detected while blurry pore-material interfaces have led to an increase of pore areas during image processing.

The tortuosity determined from the CT data had a value of 2.7, which was a lot smaller compared to the results from the FIB/SEM data. An interpretation of this value is critical due to several factors that influence the calculation. First, the resolution limit that might cause blurred boundaries. Image processing could cause separated pores to be interpreted as connected. The direction of the tortuosity calculation might influence its value. In both cases the used calculation method (centroid path tortuosity) was interpreted in all three dimensions. The orientation of the reconstruction differs from the FIB/SEM data. Another factor for the deviation might be segmentation errors in the FIB/SEM data caused by the pore-GDC interface contrast.

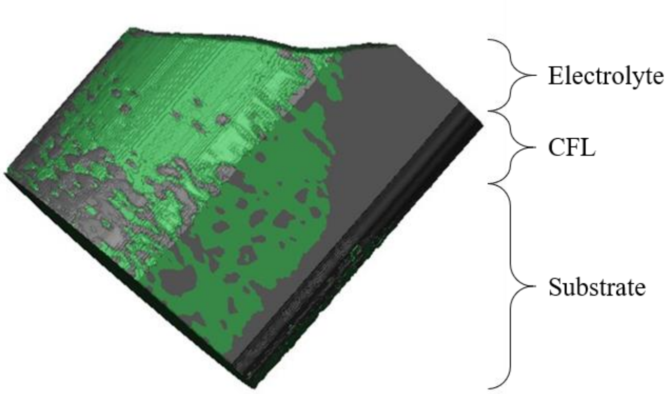

Figure 4: Distribution of pores in the reconstructed volume (3489 μm^3) that contained the electrolyte, CFL and substrate. The reconstruction still contained some segmentation artefacts in non-analyzed regions. Green: material phases, gray: pores.

Conclusion

The combination of different methods for microstructural investigations enables a broader insight into the microstructure. Visible changes and a deviation of parameters after operation might indicate the origins of the before observed cell failure.

Based on the hitherto determined microstructural parameters the microstructural reconstruction via FIB/SEM and CT seems suitable for the analysis of cell’s components. For a proceeding analysis of the methods suitability and the cell itself further parameters e.g. percolation of gas, triple phase boundaries and specific surface need to be considered. By combining CT and FIB/SEM analysis on the same specimen the reconstruction and segmentation process might be improved. The sensitivity of the different microstructural parameters regarding the size of the analyzed volume can give information about the minimum RVE size.

Acknowledgments

The authors gratefully acknowledge the funding by the Federal Ministry of Education and Research. Project: ElChFest (Elektro-chemo-mechanische Modellierung von Ceroxid-basierten Festoxidelektrolysezellen), DBB01995

References

1. C. Lenser, J. Zhang, N. Russner, A. Weber, O. Guillon and N. H. Menzler, *Journal of Power Sources*, **541,** 231505 (2022).
2. C. Lenser, H. Jeong, Y. J. Sohn, N. Russner, O. Guillon and N. H. Menzler, *J Am Ceram Soc,* **101**(2), 739–748 (2017).
3. G. Pećanac, J. Malzbender, F. Pauly, M. L. Fontaine, P. Niehoff, S. Baumann, T. Beck and L. Singheiser, *Ceramics International,* **41**(2), 2411–2417 (2015).
4. B. Rüger, J. Joos, A. Weber, T. Carraro and E. Ivers-Tiffée, *ECS Trans.,* **25**(2), 1211–1220 (2009).
5. F. Wankmüller, N. Russner, A. Weber, M. Meffert, J. Schmieg, H. Störmer, J.-C. Njodzefon, P. Lupetin, D. Gerthsen and E. Ivers-Tiffée, *ECS Trans.,* **91**(1), 501–509 (2019).
6. W. M. Harris and W. K. Chiu, *Journal of Power Sources,* **282,** 552–561 (2015).
7. M. Meffert, F. Wankmüller, H. Störmer, A. Weber, P. Lupetin, E. Ivers‐Tiffée and D. Gerthsen, *FUEL CELLS,* **20**(5), 580–591 (2020).
8. F. Wankmüller, M. Meffert, N. Russner, A. Weber, J. Schmieg, H. Störmer, T. Dickel, P. Lupetin, N. Maier, D. Gerthsen and E. Ivers-Tiffée, *J Mater Sci,* **55**(25), 11120–11136 (2020).
9. J. Joos, M. Ender, I. Rotscholl, N. H. Menzler and E. Ivers-Tiffée, *Journal of Power Sources,* **246,** 819–830 (2014).
10. J. R. Wilson, M. Gameiro, K. Mischaikow, W. Kalies, P. W. Voorhees and S. A. Barnett, *Microscopy and microanalysis : the official journal of Microscopy Society of America, Microbeam Analysis Society, Microscopical Society of Canada,* **15**(1), 71–77 (2009).
11. M. Ender, J. Joos, A. Weber and E. Ivers-Tiffée, *Journal of Power Sources*, **269,** 912–919 (2014).
12. M. Ender, J. Joos, T. Carraro and E. Ivers-Tiffée, *J. Electrochem. Soc.*, **159**(7), A972-A980 (2012).
13. J. Martín-Herrero and C. Germain, *Carbon,* **45**(6), 1242–1253 (2007).
14. J. Joos, B. Rüger, T. Carraro, A. Weber and E. Ivers-Tiffée, *ECS Trans.,* **MA2010-01**(11), 706 (2010).
15. G. Hamarneh and X. Li, *Image and Vision Computing,* **27**(1-2), 59–68 (2009).
16. S. Lou, L. Pagani, W. Zeng, X. Jiang and P. J. Scott, *Precision Engineering,* **63,** 177–186 (2020).
17. J. Schindelin, I. Arganda-Carreras, E. Frise, V. Kaynig, M. Longair, T. Pietzsch, S. Preibisch, C. Rueden, S. Saalfeld, B. Schmid, J.-Y. Tinevez, D. J. White, V.

Hartenstein, K. Eliceiri, P. Tomancak and A. Cardona, *Nature methods*, **9**(7), 676–682 (2012).